Geophys. J. Int. (2005) **162,** 9–24 doi: 10.1111/j.1365-246X.2005.02658.x

Fresnel volume georadar attenuation-difference tomography

Timothy C. Johnson, Partha S. Routh and Michael D. Knoll

Center for Geophysical Investigation of the Shallow Subsurface (CGISS), Department of Geosciences, Boise State University, 1910 *University Drive, Boise, ID* 83725 *USA. E-mail: tcj@cgiss.boisestate.edu*

Accepted 2005 April 11. Received 2005 February 25; in original form 2004 November 5

SUMMARY

Georadar attenuation-difference tomography is a useful tool for imaging temporal and spatial changes in bulk electrical conductivity due to fluid flow and other subsurface processes. The most common method of attenuation-difference tomography employs the ray approximation where waves are assumed to propagate at infinite frequency. Ray approximation causes significant model error that generates artefacts and loss of resolution in tomographic images. In this paper we propose an efficient method of computing Fresnel volume sensitivities using scattering theory. These sensitivities account for finite frequency propagation and represent the physics of electromagnetic propagation more accurately than ray theory. As expected, Fresnel volume sensitivities provide better data prediction than ray-based sensitivities. We use singular value decomposition analysis to show how and why this physical improvement allows Fresnel volume inversions to recover localized targets and resolve bulk conductivity changes better than ray-based inversions. The model basis functions and singular values corresponding to the scattering theory sensitivity kernel are similar to the exact full-waveform basis functions and singular values. The similarity of the basis functions and singular values suggests that the scattering theory inverse estimates are close to the full-waveform estimates, but they are obtained with a significant decrease in computational effort.

Key words: attenuation, electromagnetic modelling, Fréchet derivatives, inversion, scattering, tomography.

1 INTRODUCTION

Characterization of the aquifer properties that control flow and transport at scales typical of environmental and engineering problems is an area of active research. Researchers are developing innovative methods of utilizing geophysical surveys to provide additional information concerning aquifer properties and to help constrain the range of possibilities in hydrogeological parameter estimates (Hyndman *et al.* 1994; Copty & Rubin 1995; Hubbard & Rubin 2000; Day-Lewis *et al.* 2002; Barrash *et al.* 2003; Goldstein 2004). Radar attenuation-difference tomography can be used to image submetre spatial and temporal changes in bulk electrical conductivity induced by the movement of a conductively anomalous fluid such as a tracer or contaminant. Such transport information is typically sensitive to important hydrogeological properties such as porosity and hydraulic conductivity and can provide valuable information concerning the distribution of those properties.

A number of radar attenuation-difference surveys have been conducted in near-surface environments. In a series of experiments, Lane *et al.* (1999) showed how cross-well attenuation-difference data can be used to image fractures in crystalline bedrock containing saline tracer. In a follow-on study Day-Lewis *et al.* (2002) developed a novel approach to time-lapse inversion that accounts for the movement of the tracer over the course of the data collection time to improve image resolution. As with most applications of radar tomography, ray theory was used to represent the physics of electromagnetic (EM) wave propagation underlying the inverse reconstruction of the tracer distribution in each of these cases. The majority of tomographic inversions for velocity or attenuation structure (in both seismic and radar applications) are based on ray theory primarily because ray theory is well understood and computationally efficient allowing inversions of large data sets.

In ray theory, the sensitivity of pulse traveltime or attenuation to the electromagnetic properties of the medium is reduced to a line integral along the travel path between the source and the receiver. Ray-geometrical representation of wave propagation is a mathematical construct that is valid in the limiting case of infinite-frequency propagation. In finite-frequency propagation the velocities and amplitudes of waves are sensitive to some volume surrounding the fastest travel path. These sensitivity volumes were first described in terms of seismic waves by Hagedoorn (1954) and later defined as Fresnel volumes by Kravstov & Orlov (1980). Collapsing these Fresnel volumes of sensitivity to 1-D curves along the fastest travel path has several limitations. In velocity tomography, for example, rays are deflected around low-velocity regions such that high-velocity regions are preferentially sampled biasing the solution toward high velocities (Wielandt 1987; Nolet 1987). Ray theory does not account for many low-velocity regions adjacent to the fastest travel path to which corresponding traveltimes may be sensitive.

Several techniques have been developed to estimate the spatial distribution of the sensitivity of seismic arrival time to seismic velocity distributions, which are often referred to as wave path

methods (Luo & Schuster 1991; Woodward 1992; Stark & Nikolayev 1993; Vasco & Majer 1993; Vasco *et al.* 1995). Generally, the full acoustic-wave equation is used to derive the wave path sensitivity distribution associated with a particular source–receiver pair and velocity structure (Vasco & Majer 1993; Spetzler & Snieder 2004). Because they are based on a finite-frequency wave equation, the wave path sensitivities are physically more accurate than rays and include the effects of finite-frequency propagation that are neglected in ray theory. The benefits of accounting for finite-frequency effects are numerous, including the ability to image smaller-scale features and reduce tomographic artefacts. The disadvantage of wave path tomography is computational cost, since each wave path calculation requires a forward and backward propagation of a full wavefield and residual or adjoint wavefield, respectively.

In this paper we present an efficient method of computing the sensitivity of finite-frequency radar attenuation data to changes in bulk conductivity. We begin with a review of ray-based attenuation-difference tomography. Then we present the Fresnel volume sensitivity computation by defining the Fresnel volume to which attenuation data are sensitive, and then using scattering theory to compute the sensitivities within the volume. We compare the Fresnel volume sensitivity distributions to those derived by perturbing a full-waveform finite-difference solution (Holliger & Bergmann 1999) and show how the scattering theory sensitivities are more accurate than the ray-based sensitivities with a data prediction example. Following this discussion we use singular value decomposition (SVD) analysis of a synthetic example to show how this physical improvement provides better target localization in inverse estimates, giving marked improvements in tomographic resolution over ray-based inversions. By decomposing the sensitivity kernels using SVD we analyse the nature and scaling of the basis functions used to construct the inverse estimates. The slowly varying and localized composition of the scattering theory basis functions allows Fresnel volume inversions to resolve localized targets more accurately than ray-based inversions. In addition, the full-waveform and scattering theory basis functions and singular values display a similar character in both shape and magnitude, reinforcing our intuition about the validity of Fresnel-based sensitivities. The similarity between the scattering theory and full-waveform basis functions and singular values suggests that the scattering theory solution is similar to the full-waveform solution, but obtained with a significant decrease in computational effort.

2 THEORETICAL DEVELOPMENT

In this section we briefly review the ray theoretical approach to relate amplitude data to attenuation changes or perturbations in the medium. Then we discuss the Fresnel theory that relates changes in amplitudes to changes in bulk electrical conductivity within the Fresnel volume. Finally we present a method for computing the sensitivity of amplitudes to changes in the bulk conductivity of discretized cells within the Fresnel volume.

2.1 Ray theory overview

The electric field recorded at the receiver at time t_a corresponding to source–receiver configuration i is denoted by $e_{a,i}$. The ray-geometric far-field expression describing the amplitude ($A_{a,i}$) of $e_{a,i}$ is given by (Holliger *et al.* 2001; Holliger & Bergmann 2002; Day-Lewis *et al.* 2002)

$$A_{a,i} = A_{0a,i}\Theta_{sa}(\phi_i)\Theta_{ra}(\phi_i)\frac{\exp\left(-\int_l \alpha_a(s)\,ds\right)}{\int_l ds_a} \tag{1}$$

where l is the length of the ray path from source to receiver, $A_{0a,i}$ is the effective amplitude of the source at the position related to i and time t_a, α_a is the attenuation coefficient distribution at time t_a, Θ_{sa} is the source radiation pattern at time t_a, Θ_{ra} is the receiver radiation pattern at time t_a and ϕ_i is the angle between source and receiver with respect to horizontal. If radiation patterns and source amplitudes are time invariant the difference between $\ln(A_{b,i})$ and $\ln(A_{b,i})$ for a discretized medium can be expressed as

$$\ln(A_{a,i}) - \ln(A_{b,i}) = \sum_{j=1}^{N} \Delta\alpha_j \Delta r_{ij} \tag{2}$$

where $\Delta\alpha_j = \alpha_{b,j} - \alpha_{a,j}$, $\Delta r_{ij} = \Delta r_{a,ij} = \Delta r_{b,ij}$ and N is the number of cells. Eq. (2) provides a linear mapping relating the changes in attenuation between times t_a and t_b to the corresponding change in amplitude of the data. In matrix notation

$$\delta D = J^{\S}\Delta\alpha \tag{3}$$

where $\delta D = \ln(A_{a,i}) - \ln(A_{b,i})$ and $J^{\S} = \Delta r_{ij}$. Eq. (3) is the forward model for ray-based attenuation-difference tomography. In this formulation radiation pattern effects cancel by differencing the log amplitudes if the radiation patterns are time invariant. This is an attractive feature of attenuation-difference tomography because radiation patterns are typically difficult to determine. A subtle but important caveat to this result is that it was derived under the ray-geometric approximation and may not apply to the finite-frequency propagation case. Later we show that attenuation-difference data are indeed sensitive to radiation patterns in finite-frequency propagation whether radiation patterns are time invariant or not. The Fresnel zone sensitivity distributions we present here do account for radiation pattern effects assuming they are known or can be sufficiently approximated.

As a final note, some authors (e.g. Lane *et al.* 1999; Peterson 2001) derive eqs (1) and (2) slightly differently, depending primarily on the way in which $A_{a,i}$ is defined. The differences arise from the ray-geometric approximation itself which requires all of the sensitivity assigned to $A_{a,i}$ to lie upon a curve regardless of the time window within which $A_{a,i}$ is defined. Thus the definition of $A_{a,i}$ is somewhat arbitrary. In finite-frequency propagation the region in space to which $A_{a,i}$ is sensitive depends on how $A_{a,i}$ is defined. For instance, if $A_{a,i}$ is defined as the peak of the first pulse, the region in space to which $A_{a,i}$ is sensitive includes all points such that energy scattered from those points contributes to the first pulse. In the following discussion, we define $A_{a,i}$ to be sensitive to only the first Fresnel volume characterized by the period of the first half cycle of $e_{a,i}$ and the propagation velocity. Then we use scattering theory to estimate the sensitivity of amplitudes to bulk conductivity changes within the Fresnel volume assuming constant velocity propagation.

2.2 Fresnel volumes, attenuation-difference data and the sensitivity kernel

This section describes how we define attenuation-difference data and how those data are related to the first Fresnel volume characterized by the period of the first half cycle (or first pulse) and velocity of the recorded wavelet. The definition of the first Fresnel volume of constructive interference, or simply Fresnel volume, was originally given by Kravstov & Orlov (1980) and is illustrated in Fig. 1. The Fresnel volume is the region defined by

$$t_{sj} + t_{rj} - t_{sr} \leq T/2 \tag{4}$$

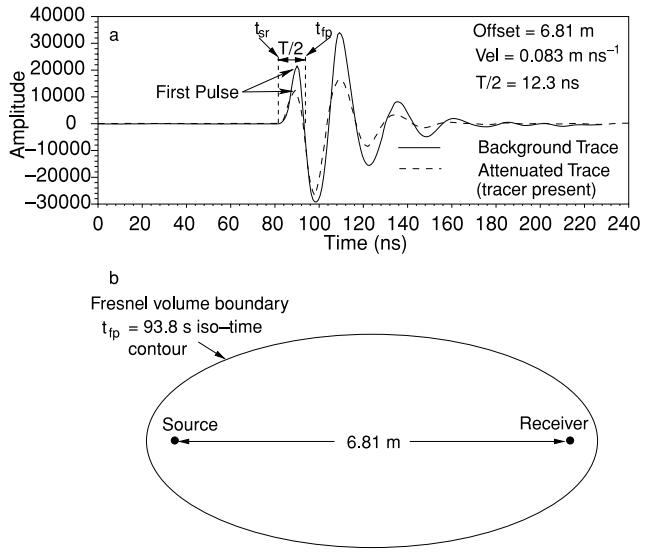

Figure 1. (a) Field examples of $e_{a,i}$ and $e_{b,i}$ gathered during a conductive tracer experiment and the corresponding theoretic Fresnel volume boundary. Note $t_{sr} \approx 81.5$ ns and $T/2 \approx 12.3$ ns are approximately equal for each trace and that the region between t_{sr} and t_{fp} includes the 'first pulse'. The velocity was estimated by dividing the offset by the time to the peak of the first pulse which is most appropriate for Fresnel zone applications (Vasco *et al.* 1995). (b) The Fresnel volume boundary bounds the region in space to which the first pulse is sensitive.

where t_{sj} is the traveltime from the source to some scattering point in space (cell j in the context of this paper), t_{rj} is the traveltime from the same point to the receiver, t_{sr} is the traveltime from source to receiver and T is the period of the propagating wave. Energy in the first $T/2$ seconds of the wavelet is only sensitive to points located within the first Fresnel volume because energy scattered from points outside of this volume arrives after time $t_{sr} + T/2$ (Červený & Soares 1992). We define $T/2$ as the length of time between the first arrival (t_{sr}) and the end of the first pulse (t_{fp}) of the arriving wavelet so that the first pulse is only sensitive to the Fresnel volume defined by T. Higher-order Fresnel zones are also sensitive to scattered energy, but computing the sensitivities for each would require an excessive computational burden and approaches the realm of full-waveform inversion where more efficient techniques (such as adjoint sensitivities) are available.

For a constant-velocity medium the Fresnel volume assumes an ellipsoidal shape with the focus points at the source and receiver positions as shown in Fig. 1. As frequency decreases the period increases and the Fresnel zone widens indicating that the energy contained in the first pulse is sensitive to a wider region in space. As frequency increases towards infinity the period approaches zero and the Fresnel zone becomes very narrow, indicating that the first pulse is sensitive only to the locus of points lying on a curve between the source and receiver as in the ray approximation. As noted earlier, we assume a constant-velocity medium so that rays are straight and Fresnel volumes are ellipsoidal. The straight-ray approximation is valid in many saturated shallow subsurface environments because velocity contrasts tend to be weak and source–receiver distances are small which limits ray bending (Lane *et al.* 1999; Day-Lewis *et al.* 2002; Buursink 2004). However, Fresnel volumes can also be computed for media with heterogeneous velocity (Spetzler & Snieder 2004).

To introduce our definition of attenuation-difference data, suppose radar data are collected between two boreholes at some background time t_a. The time domain trace of the vertical component of the electric field (E_z) corresponding to the source–receiver orientation i is given by $e_{a,i}$. A trace with the same acquisition geometry collected at some later time t_b when an electrically anomalous fluid has invaded the region between the source and receiver, is labelled $e_{b,i}$. If the fluid is conductive, the amplitude of $e_{a,i}$ will be greater than the amplitude of $e_{b,i}$ because EM wave attenuation increases with conductivity. In low-loss conditions, the relationship between the natural logarithm of EM amplitude and bulk conductivity is approximately linear (see Appendix A). With this in mind, we define the attenuation-difference data as

$$\delta D_i = \ln\left(\int_{t_{sr}}^{t_{fp}} e_{b,i}^2(t)\,dt\right) - \ln\left(\int_{t_{sr}}^{t_{fp}} e_{a,i}^2(t)\,dt\right) \tag{5}$$

where t_{sr} is the first arrival time for traces $e_{a,i}$ and $e_{b,i}$, and t_{fp} is the time to the end of the first pulse or the first zero crossing after t_{sr}. We assume that t_{sr} is equal for each trace. This assumption is valid when the change in bulk conductivity between times t_a and t_b is not extreme, because EM wave velocity is a weak function of bulk conductivity (Jackson 1999). Eq. (5) also assumes t_{fp} is constant between traces which is approximately true in the absence of a significant change in dispersion from $e_{a,i}$ to $e_{b,i}$. In other words, the conductivity change between times t_a and t_b does not significantly affect the EM wave velocity. The kinematic parts of the wave equation are equal for both times; only wave amplitudes are affected. Under this assumption, the integration limits in eq. (5) are equal for each trace. Field examples of $e_{a,i}$ and $e_{b,i}$ along with the corresponding theoretical Fresnel zone boundary (?) are shown in Fig. 1.

To construct the forward model, let the conductivity distribution at times t_a and t_b be denoted by $\sigma_a(\mathbf{r})$ and $\sigma_b(\mathbf{r})$, respectively, where $\mathbf{r}$ is the position vector. Eq. (5) then becomes

$$\delta D_i = \ln\left(\int_{t_{sr}}^{t_{fp}} e_i^2\,(\sigma_b(\mathbf{r}), t)\;dt\right) - \ln\left(\int_{t_{sr}}^{t_{fp}} e_i^2\,(\sigma_a(\mathbf{r}), t)\;dt\right). \tag{6}$$

Let $\delta\sigma(\mathbf{r})$ represent a change in the conductivity field about $\sigma_a(\mathbf{r})$ such that $\sigma_b(\mathbf{r}) = \sigma_a(\mathbf{r}) + \delta\sigma(\mathbf{r})$. Then

$$\begin{aligned}\delta D_i &= \ln\left(\int_{t_{sr}}^{t_{fp}} e_i^2\,(\sigma_a(\mathbf{r}) + \delta\sigma(\mathbf{r}), t)\;dt\right)\\ &\quad - \ln\left(\int_{t_{sr}}^{t_{fp}} e_i^2\,(\sigma_a(\mathbf{r}), t)\;dt\right).\end{aligned} \tag{7}$$

If we represent the integrals by

$$F_i(\sigma(\mathbf{r})) = \int_{t_{sr}}^{t_{fp}} e_i^2\,(\sigma(\mathbf{r}), t)\;dt, \tag{8}$$

then eq. (7) can be rewritten and expanded in Taylor series to obtain

$$\begin{aligned}\delta D_i &= \ln\left(F_i\,(\sigma_a(\mathbf{r})) + \left\langle \frac{\partial F_i\,(\sigma_a(\mathbf{r}))}{\partial\sigma_a(\mathbf{r})}, \delta\sigma(\mathbf{r})\right\rangle + O\left(\|\delta\sigma(\mathbf{r})\|^2\right)\right)\\ &\quad - \ln\left[F_i\,(\sigma_a(\mathbf{r}))\right]\end{aligned} \tag{9}$$

where $\langle\cdot,\cdot\rangle$ denotes the inner product in the spatial domain and $\partial F_i(\sigma_a(\mathbf{r}))/\partial\sigma_a(\mathbf{r})$ are Frechet derivatives. When $\delta\sigma(\mathbf{r})$ is small, second and higher-order terms of the expansion are insignificant and eq. (9) reduces to

$$\delta D_i = \left\langle \frac{1}{F_i\,(\sigma_a(\mathbf{r}))}\frac{\partial F_i\,(\sigma_a(\mathbf{r}))}{\partial\sigma_a(\mathbf{r})}, \delta\sigma(\mathbf{r})\right\rangle. \tag{10}$$

Next we express the conductivity change in discrete form as

$$\delta\sigma(\mathbf{r}) = \sum_{j=1}^{N} \delta\sigma_j \Gamma_j(\mathbf{r}) \tag{11}$$

where $\delta\sigma_j$ is the conductivity change in cell j, N is the number of cells,

$$\Gamma_j(\mathbf{r}) = \begin{cases} 1 \text{ if } \mathbf{r} \in v_j \\ 0 \text{ otherwise} \end{cases} \tag{12}$$

is the basis function used to discretize the model and v_j is the volume to which $\delta\sigma_j$ applies. Substituting this discretization into eq. (10) and taking the summation outside of the inner product gives

$$\delta D_i = \sum_{j=1}^{N} J_{ij}^{\mathrm{F}} \delta\sigma_j \tag{13}$$

where $J_{ij}^{\mathrm{F}} = \partial \ln[F_i(\sigma_a(\mathbf{r}))]/\partial\sigma_j$. Eq. (13) is the discretized forward model for Fresnel volume attenuation-difference tomography. Errors in the physics represented by J^{F} arise primarily due to the truncation of the Taylor series expansion in eq. (9) which neglects the effects of multiple scattering. This effect is evident in the expression for J_{ij}^{F} which is the sensitivity of the log first pulse energy of $e_i(\sigma_a(\mathbf{r}))$ to a single scatterer $\delta\sigma_j$.

We compute J_{ij}^{F} with the forward finite-difference operator given by

$$J_{ij}^{\mathrm{F}} = \frac{\ln\left(\int_{t_{\mathrm{sr}}}^{t_{\mathrm{fp}}} e_i^2\left(\sigma_a(\mathbf{r}) + \delta\sigma_j, t\right)\, dt\right) - \ln\left(\int_{t_{\mathrm{sr}}}^{t_{\mathrm{fp}}} e_i^2\left(\sigma_a(\mathbf{r}), t\right)\, dt\right)}{\delta\sigma_j}. \tag{14}$$

For notational convenience we drop the time dependence in e_i. We solve for $e_i(\sigma_a(\mathbf{r}))$ and $e_i(\sigma_a(\mathbf{r}) + \delta\sigma_j)$ using scattering theory and numerically compute the integrations in eq. (14). The background field $e_i(\sigma_a(\mathbf{r}))$ is computed assuming constant $\sigma_a(\mathbf{r})$ and $e_i(\sigma_a(\mathbf{r}) + \delta\sigma_j)$ is computed using the Born approximation. Next we progress through the theory and mechanics of computing J_{ij}^{F}, beginning with the integral solutions for $e_i(\sigma_a(\mathbf{r}))$ and $e_i(\sigma_a(\mathbf{r}) + \delta\sigma_j)$ including radiation pattern effects.

2.3 Fresnel volume sensitivities: theory

In this section we develop the equations describing the background and scattered fields. Notation for this development is shown in Fig. 2. We present the solution to the Helmholtz equation for a point source delta function and a small conductive scatterer, beginning with the frequency domain versions of Ampere's law and Faraday's law where the source current density is included in the $\mathbf{J}(\mathbf{r}, \omega)$ term. This is given by

$$\nabla \times \mathbf{E}(\mathbf{r}, \omega) = -i\omega\mathbf{B}(\mathbf{r}, \omega) \tag{15}$$

$$\nabla \times \mathbf{H}(\mathbf{r}, \omega) = \mathbf{J}(\mathbf{r}, \omega) + i\omega\mathbf{D}(\mathbf{r}, \omega) \tag{16}$$

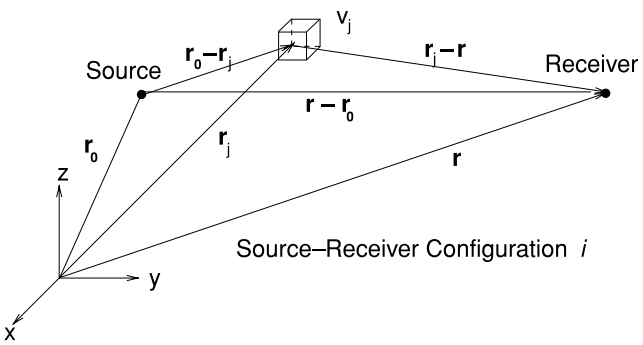

Figure 2. Diagram showing notation for the theory.

with the non-dispersive constitutive relations given by

$$\mathbf{J}(\mathbf{r}, \omega) = \sigma(\mathbf{r})\mathbf{E}(\mathbf{r}, \omega) \tag{17}$$

$$\mathbf{D}(\mathbf{r}, \omega) = \epsilon(\mathbf{r})\mathbf{E}(\mathbf{r}, \omega) \tag{18}$$

$$\mathbf{B}(\mathbf{r}, \omega) = \mu(\mathbf{r})\mathbf{H}(\mathbf{r}, \omega). \tag{19}$$

Here we assume a time harmonicity of $e^{i\omega t}$ where ω is the angular frequency and t is the time. $\mathbf{E}$ is the electric field strength, $\mathbf{B}$ is the magnetic induction, $\mathbf{H}$ is the magnetic field strength, $\mathbf{J}$ is the galvanic current density, $\mathbf{D}$ is the displacement current, $\sigma(\mathbf{r})$ is the electrical conductivity, $\epsilon(\mathbf{r})$ is the dielectric permittivity, $\mu(\mathbf{r})$ is the magnetic permeability and $\mathbf{r}$ is the position vector with respect to the system origin. We assume that variations in ϵ may be considered negligible throughout the domain and that μ may be considered constant and equal to its free space value μ_0. The propagation velocity of electromagnetic waves is a strong function of the dielectric permittivity. If variations in ϵ are small, velocity variations in the medium are also small, and ray representations of the wave propagation are approximately straight.

Substituting eq. (19), into eq. (15) and taking the curl of both sides gives

$$\nabla(\nabla \cdot \mathbf{E}(\mathbf{r},\omega)) - \nabla^2\mathbf{E}(\mathbf{r}, \omega) = -i\omega\mu_0\nabla \times \mathbf{H}(\mathbf{r}, \omega). \tag{20}$$

Under low-loss conditions the conduction currents are insignificant in comparison to the displacement currents (Jackson 1999) so that $\nabla \cdot \mathbf{E}(\mathbf{r}, \omega)$ is negligible and eq. (20) reduces to

$$\nabla^2\mathbf{E}(\mathbf{r}, \omega) = i\omega\mu\nabla \times \mathbf{H}(\mathbf{r}, \omega). \tag{21}$$

Next we substitute eqs (16) and (18) into eq. (21) to get

$$\nabla^2\mathbf{E}(\mathbf{r}, \omega) = i\omega\mu(\mathbf{J}(\mathbf{r}, \omega) + i\omega\epsilon\mathbf{E}(\mathbf{r}, \omega)). \tag{22}$$

We separate the current density into two terms, one for the current distribution in the source antenna, $(S(\mathbf{r}, \omega))$, and one for the current distribution in the medium as described by eq. (17)

$$\mathbf{J}(\mathbf{r}, \omega) = S(\mathbf{r}, \omega) + \sigma(\mathbf{r})\mathbf{E}(\mathbf{r}, \omega). \tag{23}$$

The conductivity distribution is described by

$$\sigma(\mathbf{r}) = \sigma_a(\mathbf{r}) + \delta\sigma(\mathbf{r}) \tag{24}$$

where $\sigma_a(\mathbf{r})$ is the background conductivity and $\delta\sigma(\mathbf{r})$ represents a change in the conductivity from the background. Substituting eqs (23) and (24) into eq. (22) and rearranging terms gives

$$\nabla^2\mathbf{E}(\mathbf{r}, \omega) + k^2\mathbf{E}(\mathbf{r}, \omega) = i\omega\mu_0 S(\mathbf{r}, \omega) + i\omega\mu_0\delta\sigma(\mathbf{r})\mathbf{E}(\mathbf{r}, \omega) \tag{25}$$

where $k = \sqrt{\omega^2\mu_0\epsilon - i\omega\mu_0\sigma_a(\mathbf{r})}$ is the complex wavenumber. Eq. (25) is the Helmholtz equation for the electric field due to two current sources. The first current source is $S(\mathbf{r}, \omega)$, which is the current produced in the source antenna. The second source is $\delta\sigma(\mathbf{r})\mathbf{E}(\mathbf{r}, \omega)$, which is the scattering current produced by the change in conductivity represented by $\delta\sigma(\mathbf{r})$. That is, the scatterer acts as an effective current source whose strength is proportional to the conductivity perturbation $\delta\sigma(\mathbf{r})$ and the electric field strength $\mathbf{E}(\mathbf{r}, \omega)$ within the scattering volume.

2.4 Background field solution

Since we are only solving for the z dimension of the electric field, we drop the vector notation and note that all fields and sources are given with respect to the z dimension for the rest of the derivation. We find the solution to eq. (25) by decomposing the total field into the part caused by the background conductivity $\sigma_a(\mathbf{r})$ which we denote

$E_0(\mathbf{r}, \omega)$, and the part caused by the scatterer which we denote $E_1(\mathbf{r}, \omega)$. The total field is given by $E(\mathbf{r}, \omega) = E_0(\mathbf{r}, \omega) + E_1(\mathbf{r}, \omega)$. The Helmholtz equation for $E_0(\mathbf{r}, \omega)$ is given by

$$\nabla^2 E_0(\mathbf{r}, \omega) + k^2 E_0(\mathbf{r}, \omega) = i\omega\mu_0 S(\mathbf{r}, \omega) \tag{26}$$

with the boundary conditions that $E_0\ (\mathbf{r}, \omega) \rightarrow 0$ as $\mathbf{r} \rightarrow \infty$. To find the solution to eq. (26) we assume a homogeneous background conductivity and a boundless domain, then employ the full-space Green's function for the field at $\mathbf{r}$ given a source region $\mathbf{r}'$. In three dimensions the Green's function is (Ward & Hohmann 1988)

$$G(\mathbf{r}, \mathbf{r}', \omega) = \frac{1}{4\pi|\mathbf{r} - \mathbf{r}'|} e^{-ik|\mathbf{r}-\mathbf{r}'|}. \tag{27}$$

In two dimensions the Green's function is

$$G(\mathbf{r}, \mathbf{r}', \omega) = \frac{i}{4} H_0^{(1)}(k|\mathbf{r} - \mathbf{r}'|) \tag{28}$$

where $H_0^{(1)}(k|\mathbf{r} - \mathbf{r}'\ |)$ is the Hankel function (Abramowitz & Stegun 1975). The whole space Green's function is appropriate for our problem because both the source and receiver are within the medium. If S is a point source located at $\mathbf{r}_0$ and $S(\omega)$ is the frequency domain representation of the source wavelet, then $S(\mathbf{r}_0, \omega) = \delta(\mathbf{r}_0)S(\omega)$, and the integral solution reduces to

$$E_0(\mathbf{r}, \omega) = \frac{i\omega\mu_0}{4\pi} \frac{1}{|\mathbf{r} - \mathbf{r}_0|} S(\omega) e^{-\mathbf{i}k|\mathbf{r}-\mathbf{r}_0|} \tag{29}$$

in three dimensions and

$$E_0(\mathbf{r}, \omega) = \frac{-\omega\mu_0}{4} H_0^{(1)}(k|\mathbf{r} - \mathbf{r}_0|) S(\omega) \tag{30}$$

in two dimensions.

2.5 Scattered field solution

The equation for the scattered field $E_1\ (\mathbf{r}, \omega)$ caused by a conductive scatterer at V' is given by

$$\nabla^2 E_1(\mathbf{r}, \omega) + k^2 E_1(\mathbf{r}, \omega) = i\omega\mu_0 \delta\sigma(\mathbf{r}) E(\mathbf{r}, \omega) \tag{31}$$

which has the integral solution

$$E_1(\mathbf{r}, \omega) = i\omega\mu_0 \delta\sigma_j \int_{v_j} G(\mathbf{r}, \mathbf{r}_j, \omega) E(\mathbf{r}_j, \omega)\, dv_j. \tag{32}$$

using the discretization given in eq. (11). We assume that v_j is small enough that the Green's function is approximately constant within v_j at a particular frequency, and $\delta\sigma_j$ may be taken out of the integral. We also assume v_j is small enough that $E(\mathbf{r}_j, \omega)$ is approximately constant within v_j and may also be taken out of the integral. This assumption requires that the dimensions of v_j be much smaller than the wavelength of $E\ (\mathbf{r}_j, \omega)$ (Ishimaru 1978). Under these conditions eq. (32) reduces to

$$E_1(\mathbf{r}, \omega) = i\omega\mu_0 \delta\sigma_j v G(\mathbf{r}, \mathbf{r}_j, \omega) E(\mathbf{r}_j, \omega) \tag{33}$$

where $\mathbf{r}_j$ denotes the position of the centroid of v_j for the remainder of the derivation.

To obtain the scattered field solution in eq. (33) we replace $E(\mathbf{r}_j, \omega)$ with the background field solution assuming that $E(\mathbf{r}_j, \omega) \approx E_0\ (\mathbf{r}_j, \omega)$, or apply the Born approximation (Ishimaru 1978). After substitutions this gives

$$E_1(\mathbf{r}, \omega) = -\frac{\omega^2\mu_0^2 v_j \delta\sigma_j}{16\pi^2|\mathbf{r} - \mathbf{r}_j||\mathbf{r}_j - \mathbf{r}_0|} e^{-ik(|\mathbf{r}-\mathbf{r}_j|+|\mathbf{r}_j-\mathbf{r}_0|)} S(\omega). \tag{34}$$

in three dimensions.

The total electric field measured at the receiver is

$$E(r, \omega) = \frac{i\omega\mu_0}{4\pi} \frac{1}{|\mathbf{r} - \mathbf{r}_0|} S(\omega) e^{-ik|\mathbf{r}-\mathbf{r}_0|} - \frac{\omega^2\mu_0^2 v_j \delta\sigma_j}{16\pi^2|\mathbf{r} - \mathbf{r}_j||\mathbf{r}_j - \mathbf{r}_0|} e^{-ik(|\mathbf{r}-\mathbf{r}_j|+|\mathbf{r}_j-\mathbf{r}_0|)} S(\omega). \tag{35}$$

Eq. (35) is the fundamental equation used in computing the EM field due to a conductive perturbation in a homogeneous medium. It is the total field solution for a single scatterer under the Born approximation. Note that for scatterers located along the ray, the complex exponential terms of the background and scattered fields are equivalent. However, the background field term contains the complex number i indicating that the background field is phase shifted by 90° with respect to the scattered field for scatterers along the ray. This becomes an important factor when describing the properties of the sensitivity distributions shown in the results section. In the next section we show how this equation is used to approximate the Fresnel volume sensitivities.

3 SENSITIVITY COMPUTATION AND ANALYSIS

3.1 Sensitivities using scattering theory

We begin by discretizing the 3-D computational domain into small cells. The volume v_j of cell j must be small enough that the electric field and the Green's function within the cell are approximately constant at any moment in time so that eq. (34) holds. We show in Section 4.1 that for a 100 MHz Ricker wavelet with a corresponding dominant wavelength of approximately 1 m, the integral solution presented here matches well with the finite-difference solution when the cells are cubes with 0.25 m sides, or about 25 per cent of the dominant wavelength. Once a discretization is chosen, the centre point of cell j is used to compute $|\mathbf{r}_j - \mathbf{r}_0|$ and $|\mathbf{r} - \mathbf{r}_j|$ in the solution for the scattered field caused by cell j.

The time domain source term $s(t)$ is a shifted Ricker wavelet defined by

$$s(t) = \left[1 - 2\pi^2 f_0^2 (t - t_s)^2\right] \exp\left[-\pi^2 f_0^2 (t - t_s)^2\right] \tag{36}$$

where f_0 is the dominant source frequency and t_s is a time shift to ensure causality. Once the source function is defined, $\mathbf{E}_0(\mathbf{r}, \omega)$ is computed by eq. (29) and $e_i(\sigma_a(\mathbf{r}))$ is computed by

$$e_i(\sigma_a(\mathbf{r})) = \mathcal{F}^{-1}\left(E_0(\mathbf{r}, \omega)\right) \tag{37}$$

where $\mathcal{F}^{-1}()$ is the time-frequency inverse Fourier transform.

Eq. (37) is the background field solution for a point source with an isotropic radiation pattern. To illustrate the implementation of more complicated radiation patterns, consider the general source and receiver radiation patterns $\Theta_s(\phi_i)$ and $\Theta_r(\phi_i)$ where ϕ_i is the source–receiver angle with respect to horizontal associated with the ith source–receiver configuration. Then the background field is given by

$$e_i(\sigma_a(\mathbf{r})) = \mathcal{F}^{-1}\left(E_0(\mathbf{r}, \omega)\right) \Theta_s(\phi_i) \Theta_r(\phi_i). \tag{38}$$

In this paper we assume dipole-type radiation patterns such that $\Theta_s\ (\phi_i) = \Theta_r(\phi_i) = \cos\ (\phi_i)$. The final step with respect to the background field is to integrate $[e_i(\sigma_a\ (\mathbf{r}))]^2$ over the first pulse. We do this with a simple algorithm that identifies the arrival time t_{sp} and the end of the first pulse t_{fp}, as shown in Fig. 3, and then integrates $[e_i(\sigma_a\ (\mathbf{r}))]^2$ numerically between these limits.

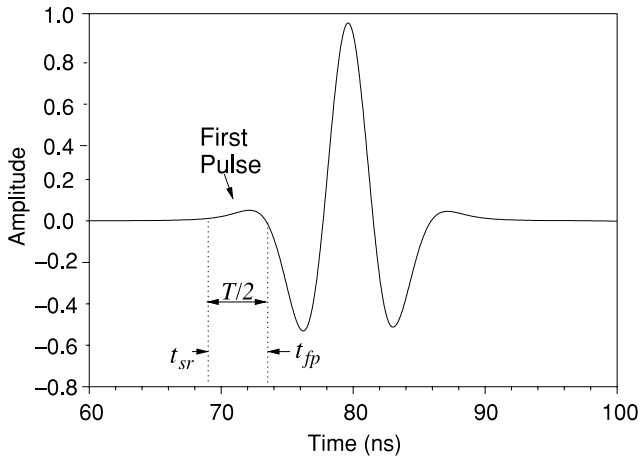

Figure 3. Integration limits of background wavelets computed with the scattering theory solution. The algorithm determines $t_{\rm fp}$ by finding the zero crossing of the first pulse. The first arrival time $t_{\rm sp}$ is determined by picking the time where the wavelet amplitude exceeds a user-defined value. The first pulse time $T/2$ is slightly greater than 4 ns in this case. In practice this wavelet would be used to compute the Fresnel volume sensitivities of a field trace with a first pulse time of approximately 4 ns.

For those cells within the Fresnel volume corresponding to shot receiver orientation i, the total field for each scatterer $e_i(\sigma_a(\mathbf{r}) + \delta\sigma_j)$ is computed by adding the scattered field solution to the background field solution. The scattered field solution, which we label $e_{1i}(\sigma_a(\mathbf{r}) + \delta\sigma_j)$, is computed in a manner analogous to the computation for $e_i(\sigma_a(\mathbf{r}))$. First $E_1(\mathbf{r}, \omega)$ is computed by eq. (34). For isotropic radiation and sensitivity pattern, $e_{1i}(\sigma_a(\mathbf{r}) + \delta\sigma_j)$ is given by

$$e_{1i}(\sigma_a(\mathbf{r}) + \delta\sigma_j) = \mathcal{F}^{-1}\left(E_1(\mathbf{r}, \omega)\right). \tag{39}$$

If we assume isotropic scattering and source and receiver radiation patterns given by $\Theta_{\rm s}(\phi_{sij})$ and $\Theta_{\rm r}(\phi_{rij})$, then $e_{1ij}(\sigma_a(\mathbf{r}) + \delta\sigma_j)$ is given by

$$e_{1i}(\sigma_a(\mathbf{r}) + \delta\sigma_j) = \mathcal{F}^{-1}\left(E_1(\mathbf{r}, \omega)\right)\Theta_{\rm s}(\phi_{sij})\Theta_{\rm r}(\phi_{rij}) \tag{40}$$

where ϕ_{sij} and ϕ_{rij} are the vertical angles between cell j and the source and receiver respectively for source–receiver configuration i. Eq. (40) explicitly shows how the amplitude of the scattered field is affected by the radiation patterns and the position of the scatterer with respect to the source and receiver. The total field is given by

$$e_i(\sigma_a(\mathbf{r}) + \delta\sigma_j) = e_i(\sigma_a(\mathbf{r})) + e_{1i}(\sigma_a(\mathbf{r}) + \delta\sigma_j). \tag{41}$$

Finally, we integrate over the first pulse of $e_i(\sigma_a(\mathbf{r}) + \delta\sigma_j)^2$ as discussed above and compute J_{ij}^F as shown in eq. (14). A similar procedure can be used to compute $J^{\rm F}$ for the 2-D problem using the 2-D Green's function shown in eq. (28) if the source is 2-D. Because we are using a 3-D source function, we compute the 2-D sensitivities by integrating the 3-D $J^{\rm F}$ along the strike dimension.

3.2 Finite-difference approach

We verify the analytical solutions for $e_i(\sigma_a(\mathbf{r}))$, $e_i(\sigma_a(\mathbf{r}) + \delta\sigma_j)$ and $e_{1i}(\sigma_a(\mathbf{r}) + \delta\sigma_j)$ by comparison with the 2-D finite-difference time-domain solution to the vertical component of the EM field given by Holliger & Bergmann (2002). They also assume dipole-type antennas with a time-shifted Ricker source wavelet so the results are directly comparable. The finite-difference solutions for the background and total fields are computed directly. Then the scattered field is determined by $e_{1i}(\sigma_a(\mathbf{r}) + \delta\sigma_j) = e_i(\sigma_a(\mathbf{r}) + \delta\sigma_j) - e_i(\sigma_a(\mathbf{r}))$ for comparison with the scattering theory solution. We also use the finite-difference solution to produce synthetic data to compare with the Fresnel zone and straight-ray forward and inverse solutions. Finally, we compute the full-waveform sensitivity distribution about the synthetic solution in a manner analogous to the Fresnel zone computations. However, in this case $\sigma_a(\mathbf{r})$ represents the true conductivity distribution so that the sensitivities are computed about the solution. We denote the full-waveform sensitivity distribution by $J^{\rm FW}$ and use $J^{\rm FW}$ as the benchmark solution to compare the properties of $J^{\rm S}$ and $J^{\rm F}$ in the SVD analysis.

3.3 Synthetic data inversion and SVD analysis

One of the goals of this paper is to show quantitatively how the Fresnel zone sensitivity kernel $J^{\rm F}$ represents the physics of wave propagation better than the ray theory sensitivity kernel $J^{\tilde{\rm S}}$, and to show how inverse solutions produced using $J^{\rm F}$ result in better-resolved images with fewer artefacts. We do this for a synthetic test case by comparing the properties of $J^{\rm FW}$ with $J^{\rm F}$ and $J^{\rm S}$ using SVD analysis. We consider the case where there are more parameters than data and regularization is introduced only by truncating the number of basis functions in the solution obtained from the SVD analysis. No additional *a priori* constraints are imposed in the inverse solution. To make the analysis directly comparable, we produce synthetic data under low-loss conditions so that the relationship between attenuation coefficient and bulk conductivity is approximately linear, and the straight-ray sensitivity kernel may be given as (see Appendix A)

$$J^{\rm S} = \frac{J^{\tilde{\rm S}}\sqrt{\mu/\epsilon}}{2} \tag{42}$$

where $J^{\tilde{\rm S}}$ is the straight-ray Jacobian matrix shown in eq. (3). Under this transformation, $J^{\rm S}$, $J^{\rm F}$ and $J^{\rm FW}$ have the same units.

The objective of the inversion is to find an optimal set of conductivity perturbations ($\delta\sigma_{\rm c}$) that minimizes in the least-squares sense the difference between the data (δD) and the model output ($J\delta\sigma_{\rm c}$). To examine the effect of scattering theory and straight-ray physics on the inverse solution we avoid incorporating *a priori* information into the solution, and therefore only data misfit contributes to our objective function. The objective function can be written as

$$\min ||J\delta\sigma_c - \delta D||^2. \tag{43}$$

The standard least-squares solution is obtained by solving the normal equations given by

$$J^{\rm T}J\delta\sigma = J^{\rm T}\delta D. \tag{44}$$

Using SVD, J can be decomposed into (Golub & Van Loan 1983)

$$J = U\Lambda V^{\rm T} \tag{45}$$

where U is a matrix of singular vectors in the data space, V is a matrix of singular vectors (or basis functions) in the model space and Λ is an ordered diagonal matrix of decreasing singular values. For the model geometry in our synthetic example the reconstructed solution $\delta\sigma_{\rm c}$ is given by

$$\delta\sigma_{\rm c} = VV^{\rm T}\delta\sigma = V\Lambda^{-1}U^{rmT}\delta D \tag{46}$$

where $VV^{\rm T}$ is the resolution matrix and $\delta\sigma$ is the exact solution. Eq. (46) can be written alternatively as

$$\delta\sigma_{\rm c} = \sum_{j=1}^{k}\left(\frac{U_j^{\rm T}\delta D}{\Lambda_j}\right)V_i \tag{47}$$

where k is the truncation index. For example, if $\lambda_{k+1} \approx 0$ then k would be the maximum truncation index for the truncated SVD solution and the resolution matrix will not be identity (i.e. $VV^{\mathrm{T}} \neq I$). Eq. (47) shows that the reconstructed solution is a linear combination of basis functions V_i weighted by the coefficients $U_j^{\mathrm{T}}\delta D/\Lambda_j$. To compare the scattering theory and ray-based Jacobian matrices with the full-waveform Jacobian matrix, we show the model basis functions and singular values as a function of truncation index. The full-waveform Jacobian matrix represents the true physics as well as possible and is the benchmark with which we compare the scattering theory and ray-based Jacobian matrices. The rigour of either method is evaluated based on how well the basis function and singular value properties match those of their full-waveform counterparts. We also show Fresnel zone and ray-based $\delta\sigma_{\mathrm{c}}$ distributions at several truncation points to illustrate how the solution is being constructed as more basis functions are included in the solution. This analysis yields insight into how and why the physical improvement represented by the Fresnel zone inversion provides a more resolved solution with fewer artefacts than the ray-based inversion.

4 RESULTS AND DISCUSSION

4.1 Sensitivity distributions, radiation pattern effects, and data predictions

Fig. 4 shows the scattering theory and finite-difference solutions for $e_i(\sigma(\mathbf{r}))$, $e_i(\sigma(\mathbf{r}) + \delta\sigma_j)$ and $e_{1i}\ (\sigma(\mathbf{r}) + \delta\sigma_j)$. The finite-difference

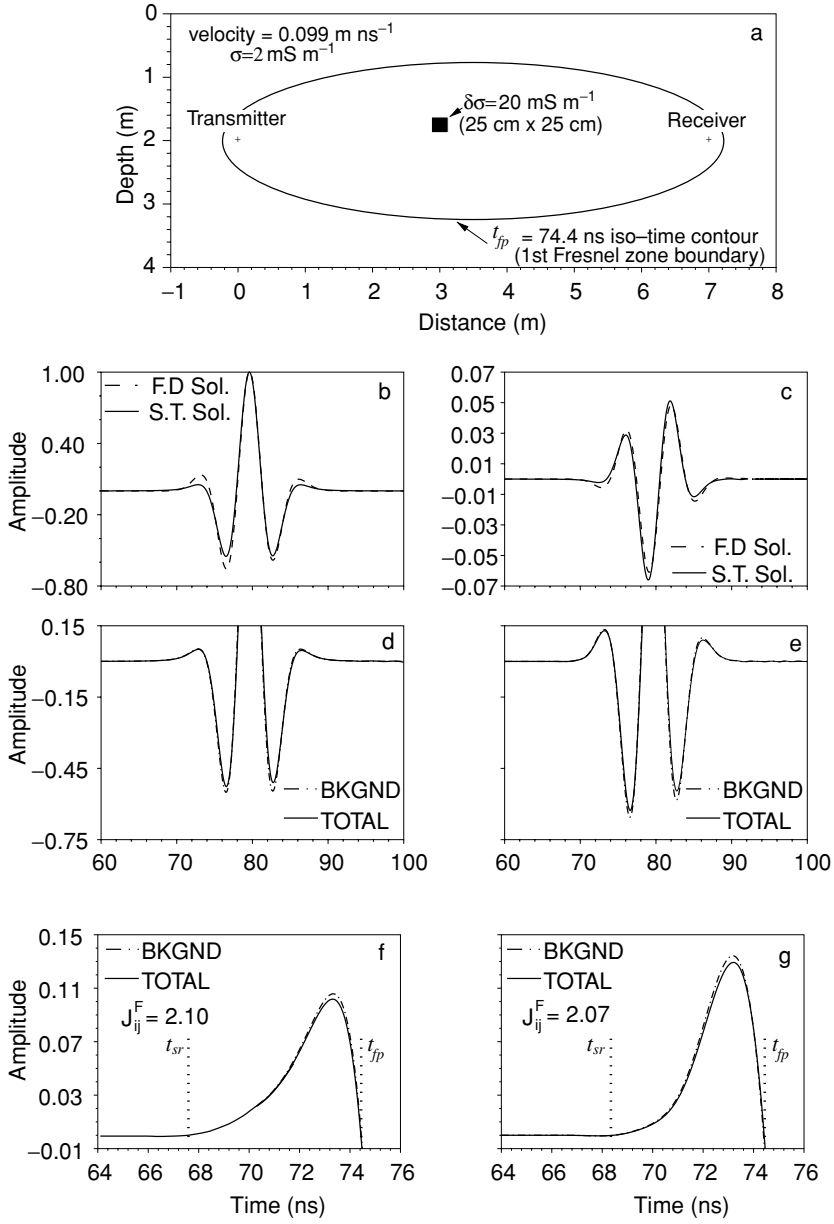

Figure 4. Scattering theory (S.T.) and finite-difference (F.D.) solution comparisons. (a) Source position, receiver position, scattering size, magnitude and Fresnel volume boundary. (b) Scattering theory and finite-difference background solutions $e_i\ (\sigma_a\ (\mathbf{r}))$. (c) Scattering theory and finite-difference scattered solutions $e_{1i}(\sigma_a(\mathbf{r}) + \delta\sigma_j)$. (d) Scattering theory background and total field solutions. (e) Finite-difference background and total field solutions. (f) Scattering theory background and total field first pulse, integration limits and sensitivity estimation. (g) Finite-difference background and total field first pulse, integration limits and sensitivity estimation. The sensitivity estimations are comparable in each case.

grid consists of 5 cm^2 cells which are small enough to effectively remove numerical dispersion (Holliger & Bergmann 2002). A large $\delta\sigma_j$ was chosen to illustrate the difference in first-pulse amplitude between $e_i(\sigma(\mathbf{r}))$ and $e_i(\sigma(\mathbf{r}) + \delta\sigma_j)$ and to show the close proximity of the scattering theory solution to the finite-difference solution when $\delta\sigma_j$ is large. Although the conductivity difference is an order of magnitude greater than the background conductivity, the relative background and scattered field amplitudes are approximately equal for each solution. This result suggests that for the case of a single scatterer the second- and higher-order terms of eq. (9) are insignificant, and that most of the sensitivity errors are due to multiple scattering effects that become operative in heterogeneous conductivity distributions. Although the Fourier amplitudes of each solution are identical, there is a slight difference in the phase of the solutions which is due to the manner in which the source functions are implemented. These phase differences are of little consequence in the computation of J^{F} because the phase of each background and scattered solution depends on the phase of the source function such that the effect on the first-pulse sensitivity of the total solution is independent of phase. Thus, the sensitivity of the change in first-pulse energy to the scatterer is comparable between the scattering theory and finite-difference solutions.

Fig. 5 shows the 2-D distribution of Fresnel zone sensitivities and compares the scattering theory and finite-difference sensitivity distributions about a homogeneous background. The distributions are similar, with peak sensitivities near the source and receiver positions. Sensitivities are depressed along the ray path where ray theory concentrates all of the sensitivity. The largest errors in the sensitivity approximations occur near the source and receiver positions where equipotential surface curvatures are large and the assumption of a constant electric field within cells may be violated. Reducing the size of the cells near the antenna positions will reduce these errors. Larger errors may occur when the model is heterogeneous and multiple scattering becomes operative. In practical applications the true conductivity distribution will always be heterogeneous (or else there would be nothing to image) so that multiple scattering errors arise in the scattering theory sensitivities. We expect the finite-difference sensitivities to be more accurate than the scattering theory sensitivities in this case. However, the scattering theory sensitivities are more efficient to compute. In Fig. 5 the finite-difference sensitivity distribution takes approximately 90 min to compute whereas the scattering distribution takes approximately 1 s on the same computer. As a result, we parallelized the finite-difference forward code to expedite the computation of J^{FW}. We will show in the SVD analysis that the scattering theory sensitivities in J^{F} have properties (i.e. singular values and basis functions) similar to the exact sensitivities in J^{FW} computed with the finite-difference solution. This suggests that under the appropriate circumstances J^{F} can provide inverse estimates similar to those provided by J^{FW} with a dramatic increase in computational efficiency.

Scattering theory and finite-difference sensitivity distributions for a high-angle source–receiver configuration and dipole-type radiation pattern are shown in Fig. 6. The dipole radiation pattern causes the sensitivity distribution to skew toward cells that are oriented horizontally with respect to the source and receiver. Fig. 7 shows isosurface and cross-sectional representations of 3-D scattering theory Fresnel volume sensitivity distributions for isotropic and dipole-type radiation patterns. In the isotropic case the sensitivity distribution is symmetric about the corresponding straight-ray and insensitive along the ray path, assuming a doughnut-type shape in planes normal to the ray path. Fig. 7(b) show the sensitivity distribution when dipole type radiation patterns are implemented. The

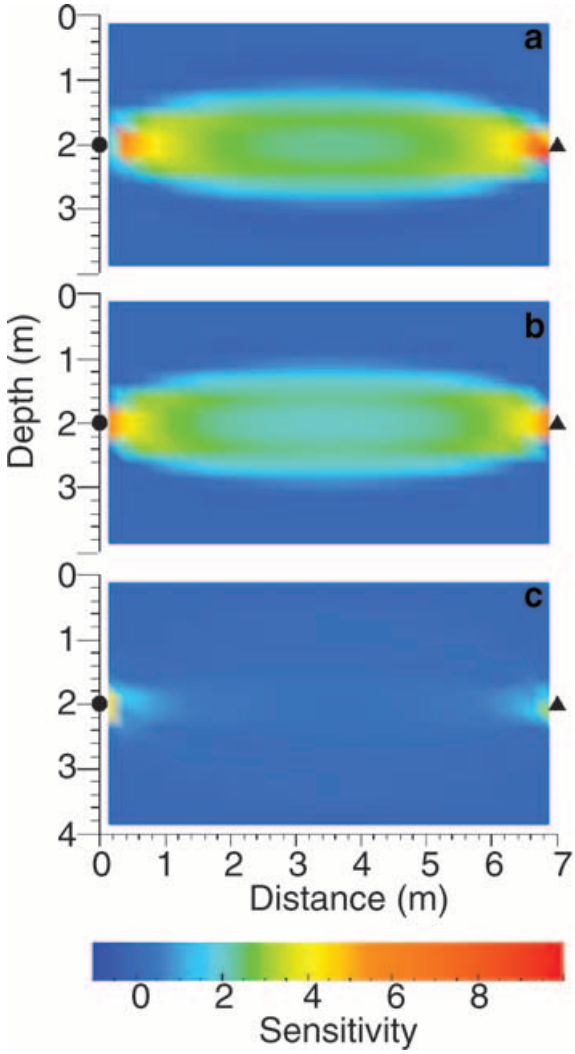

Figure 5. Scattering theory and finite-difference Fresnel zone sensitivity distribution comparisons for 100 MHz source, background conductivity of 0.002 S m^{-1} and a scattering strength of $\delta\sigma = 0.0001$ S m^{-1} . Cell sizes are 0.25 cm for the scattering theory solution and 0.05 cm for the finite-difference solution. (a) Finite-difference sensitivity distribution for a homogeneous background. (b) Scattering theory sensitivity distribution. (c) Sensitivity error

distribution normal to the corresponding ray path assumes a horseshoe-type shape with the maximum sensitivities skewed towards horizontal.

As discussed in Section 2.1, differencing attenuation data causes radiation pattern effects to cancel when waves propagate as rays and radiation patterns are time invariant. This is only true in infinite-frequency propagation. Figs 6 and 7 show that finite-frequency attenuation differences are influenced by radiation pattern effects because the sensitivities of attenuation differences within the Fresnel volume are influenced by radiation patterns. Assuming that radiation patterns cancel through data differencing could cause significant forward model error and inverse solution artefacts in the straight-ray case. Scattering theory sensitivities can account for these effects if the radiation patterns are known or can be adequately approximated.

Another interesting aspect of the sensitivity distributions are the depressed sensitivities along the ray path in the 2-D case and the

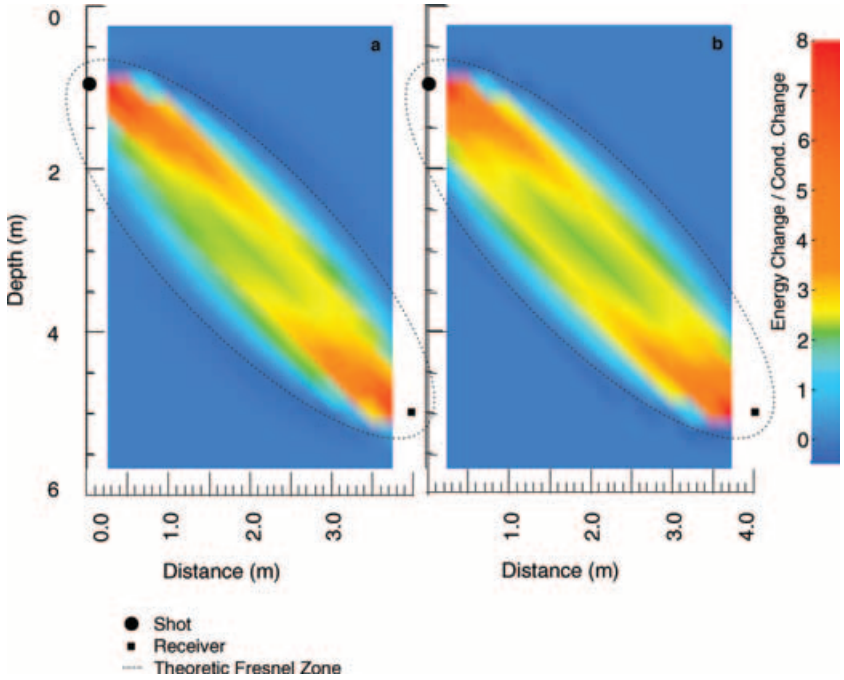

Figure 6. High-angle Fresnel zone sensitivities showing the effect of a dipole-type radiation pattern. (a) Finite-difference sensitivity distribution. (b) Scattering theory sensitivity distribution.

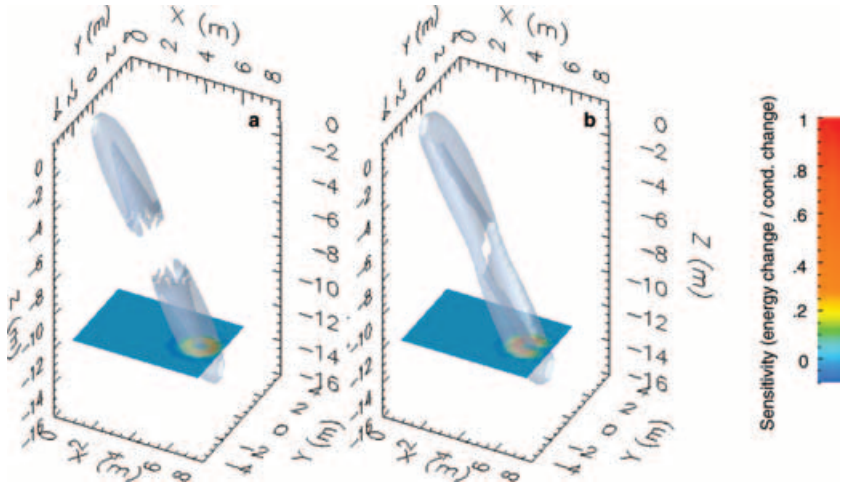

Figure 7. 3-D scattering theory Fresnel volumes. Isosurfaces are at a sensitivity value of 1. Source $(x, y, z) = (1, 0, -1)$ m. Receiver $(x, y, z) = (7, 0, -15)$. The cross-section is z-normal at $z = -12$ m. (a) Sensitivities assuming an isotropic radiation pattern. (b) Sensitivities assuming a dipole-type source and receiver radiation patterns.

complete insensitivity along the ray path in the 3-D case. Similar velocity sensitivity distributions have been documented in seismic wave theory (Marquering *et al.* 1999). However, the reason for the insensitivity along the ray is different in this case. In the seismic case, energy scattered from points along the ray arrives in phase with the background wavelet so that only amplitudes are affected in the total wavelet (Hung *et al.* 2001). Thus there is no traveltime shift required to correlate the background and total wavelets and no sensitivity along the ray. In the EM wave propagation case, the scattered wavelet from a conductive scatterer arrives 90° out of phase with the background wavelet for points along the ray. This is illustrated by the equation for the total field given in eq. (35). For points along the ray the complex exponential terms in the background and scattered wavelets are equal. However, the background wavelet coefficient contains the complex number i and the scattered wavelet does not. Thus the scattered wavelet is phase shifted with respect to the background wavelet for points along the ray. This phase shift causes equal amounts of constructive and destructive energy to be added to the first pulse of the background wavelet, which is the cause of the insensitivity of conductive scatterers along the ray. The effect is displayed graphically in Fig. 8 which shows a background and scattered wavelet for a scatterer placed on the ray. The zero-sensitivity region can be distorted when radiation patterns are anisotropic, as shown in Fig. 7.

To compare the accuracy of the Fresnel zone and ray-based forward models, we used the finite-difference solution to generate a set of background traces for a homogeneous medium. These traces correspond to $e_{a,i}$ in eq. (5). Next we added conductive anomalies

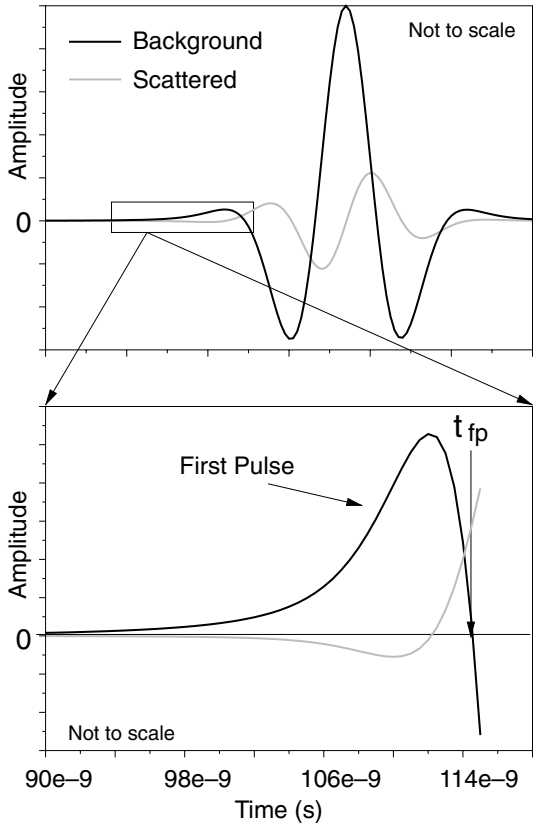

Figure 8. Example background and scattered wavelet for a scatterer located along the ray path. The scattered wavelet is phase shifted and adds approximately equal amounts of constructive and destructive energy to the first pulse of the background wavelet, resulting in depressed sensitivity along the ray.

representing a tracer or contaminant plume (i.e. $\delta\sigma(\mathbf{r})$) to the background and generated the traces representing $e_{b,i}$. The 'true' synthetic data δD_i were then computed by eq. (5). To compute the Fresnel zone and straight-ray predictions of δD_i, (δD_i^{F} and δD_i^{S} respectively), we computed J^{F} and J^{S} and then the predicted data by

$$\delta D_i^{\mathrm{F}} = \sum_j J_{ij}^{\mathrm{F}} \delta\sigma_j \quad \text{and} \quad \delta D_i^{\mathrm{S}} = \sum_j J_{ij}^{\mathrm{S}} \delta\sigma_j. \tag{48}$$

Fig. 9 shows the $\delta\sigma$ distribution, the true data cross-plot, and the Fresnel zone and ray-based data prediction and prediction error cross-plots.

The data prediction and prediction error cross-plots in Fig. 9 are useful for evaluating the accuracy of each model. If the model performs well, both the shape and magnitude of the predicted data cross-plot will match that of the true data cross-plot. The Fresnel zone model tends to over-predict some of the data, but in general the shape of the distribution matches that of the true data reasonably well. In comparison, the ray-based model significantly mis-predicts both the magnitude and the distribution of the data. Thus, the Fresnel zone inverse solution will fit the data well when the inverse solution $\delta\sigma_{\mathrm{c}}$ is approximately equal to the true solution $\delta\sigma$. This is not the case for the straight-ray model, and the straight-ray inversion may impose artefacts in order to fit the data.

This point is further illustrated by a thought experiment. Fig. 10 compares J^{F} and J^{S} versus cell number for a particular shot–receiver pair. The total integrated sensitivity for each case is approximately equal. This is a requirement since, under low-loss conditions, the Fresnel zone and straight-ray models must predict the same data for large-scale $\delta\sigma(\mathbf{r})$ distributions, such as when $\delta\sigma(\mathbf{r})$ is homogeneous (Spetzler & Snieder 2004). However, because the ray-based sensitivities are concentrated along the ray, cells through which the ray passes have erroneously high sensitivities, causing the large data over-predictions shown in Fig. 9(d). Cells within the Fresnel zone but not directly in the path of the ray have zero sensitivity in the ray-based case, which is erroneously low, causing the data underpredictions shown in Fig. 9(d). Now consider the case of the two shot–receiver pairs shown in Fig. 10(b). In the ray 1 case, the ray does not directly pass through the conductive anomaly.

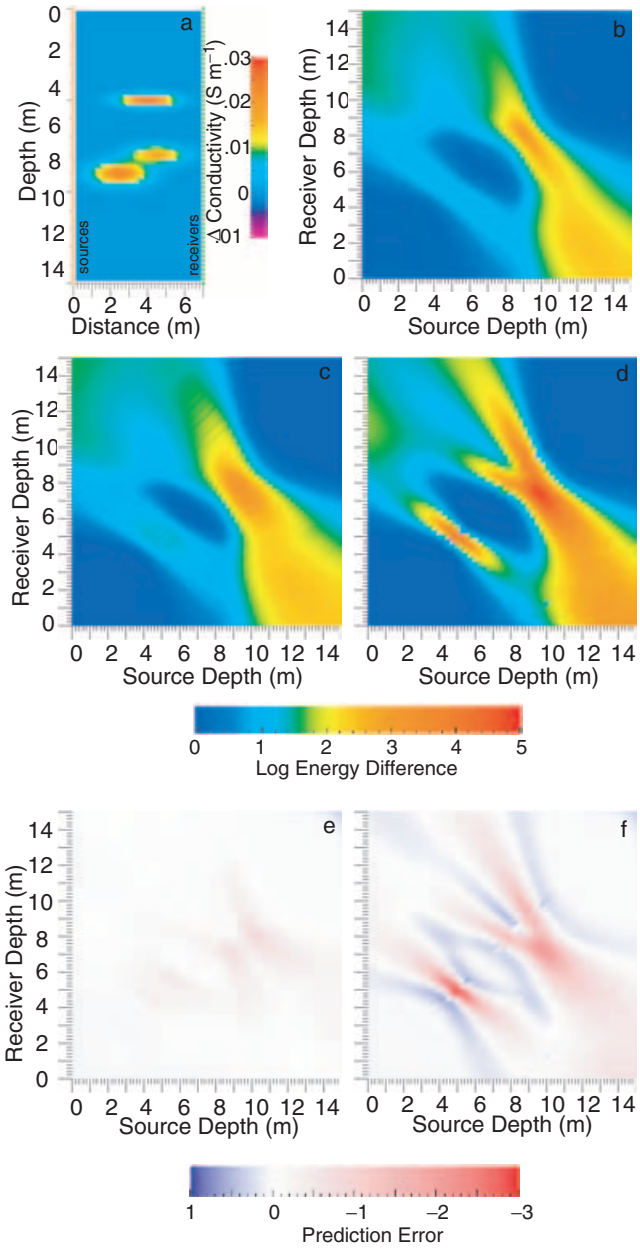

Figure 9. Fresnel zone and ray-based data predictions. The background conductivity is 0.002 S m^{-1}. (a) The conductivity model $\delta\sigma(\mathbf{r})$. Borehole separation is 7 m. Boreholes are 15 m deep with sources and receivers every 0.25 m. (b) Finite-difference-generated data (δD_i) cross-plot. (c) Scattering theory data prediction (δD_i^{F}) cross-plot. (d) Ray-based data prediction (δD_i^{S}) cross-plot. (e) Scattering theory prediction error ($\delta D_i^{\mathrm{F}} - \delta D_i$). (f) Ray-based model prediction error ($\delta D_i^{\mathrm{S}} - \delta D_i$).

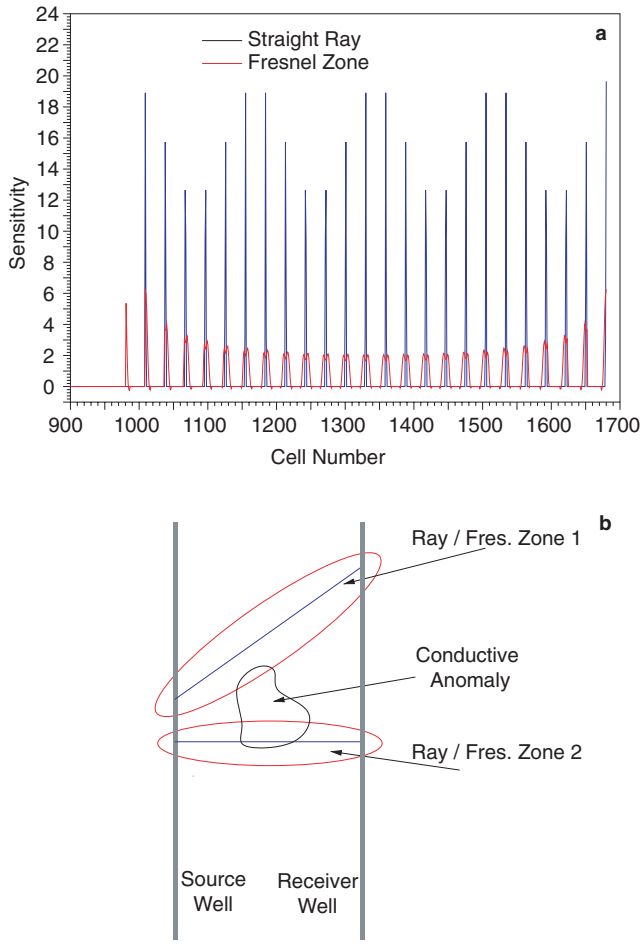

Figure 10. (a) Fresnel zone versus straight-ray sensitivity magnitudes versus parameter number for a particular source–receiver pair. The total sensitivity for each case is equal. Straight-ray sensitivities are too large and spiked at cells through which the ray passes. (b) Schematic of source–receiver configurations, the associated straight-ray and Fresnel zone sensitivity boundaries, and a conductive anomaly.

However, the anomaly is within the Fresnel zone so the datum associated with that ray will be affected by the anomaly. In order to fit the datum associated with that ray, the ray-based inversion must smear the boundary of the anomaly to the ray which results in a loss of spatial resolution. The ray-based inversion is forced to expand the boundaries of the estimated anomaly to fit the data associated with rays passing near the true boundaries. This smearing is a consequence of model error and increases as frequency decreases, Fresnel zones become wider, and the ray-geometric approximation becomes less valid.

Next consider ray 2 in Fig. 10(b). In this case, the ray passes directly through the anomaly and the anomaly encompasses only a part of the Fresnel zone. The ray-based inversion is not forced to expand the boundaries of the estimated plume to fit the datum in this case, but because the sensitivities along the ray are too high, the cells through which this ray passes must have values of conductivity change that are too low or oscillatory in order to fit the datum associated with the ray. The overall result in the inverse estimate is that the estimated values of conductivity change are too low. The SVD solutions we will show illustrate both the boundary smearing effect and the low predictions caused by model error in the ray-based inversions.

4.2 SVD analysis

To illustrate how physical improvement in the Fresnel zone representation of wave propagation leads to more accurate and resolved attenuation-difference estimates, we conducted a SVD analysis of a synthetic case. We constructed J^{FW}, J^{F} and J^{S} for the model geometry shown in Fig. 9(a), only with sources and receivers at 1 m intervals from 0 to 15 m for a total of 256 data points. Recall J^{FW}, J^{F} and J^{S} are respectively the full waveform, scattering theory and ray-based Jacobian matrices. J^{FW} was computed about the true solution and contains the exact sensitivities. Parameter cells are 0.25 m squares for a total of 1680 parameters. Fig. 11 shows the non-zero singular values corresponding to J^{FW}, J^{F} and J^{S} as a function of increasing index number. The spectrum shows that the singular values begin at approximately the same magnitude of 8×10^4. The straight-ray singular values initially drop and then cluster around the value of approximately 10^4 whereas the full-waveform and scattering theory singular values steadily decrease, displaying a decay in the singular value spectrum. Based on the singular values alone, we might conclude that the ray-based method will provide a better solution, since the singular values for the ray-based case are greater than the singular values for the scattering theory case. This would be true if the nature of the basis functions V_i were comparable between the two methods. However, these basis functions show a significantly different character. Fig. 12 shows the basis functions corresponding to selected singular values in Fig. 11. The full-waveform and scattering theory basis functions are similar, beginning with a smooth slowly varying nature and gradually become more oscillatory with increasing index. In addition, these basis functions display more localization than the straight-ray counterparts. For example, the first basis function for the straight-ray case is essentially providing a

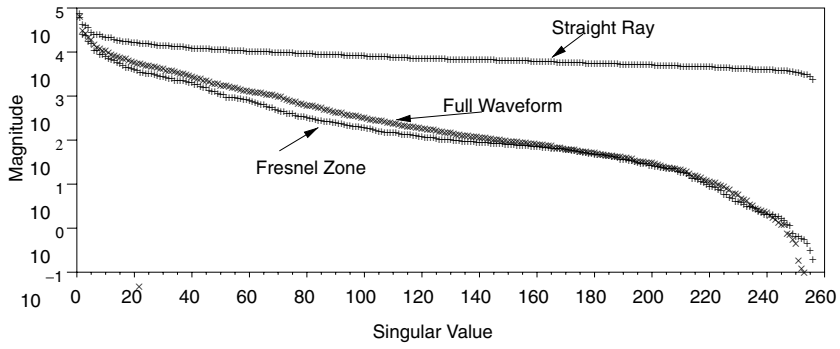

Figure 11. Singular value comparison for full-waveform (J^{FW}_{ij}), scattering theory (J^{F}_{ij}) and ray-based (J^{S}_{ij}) decomposition.

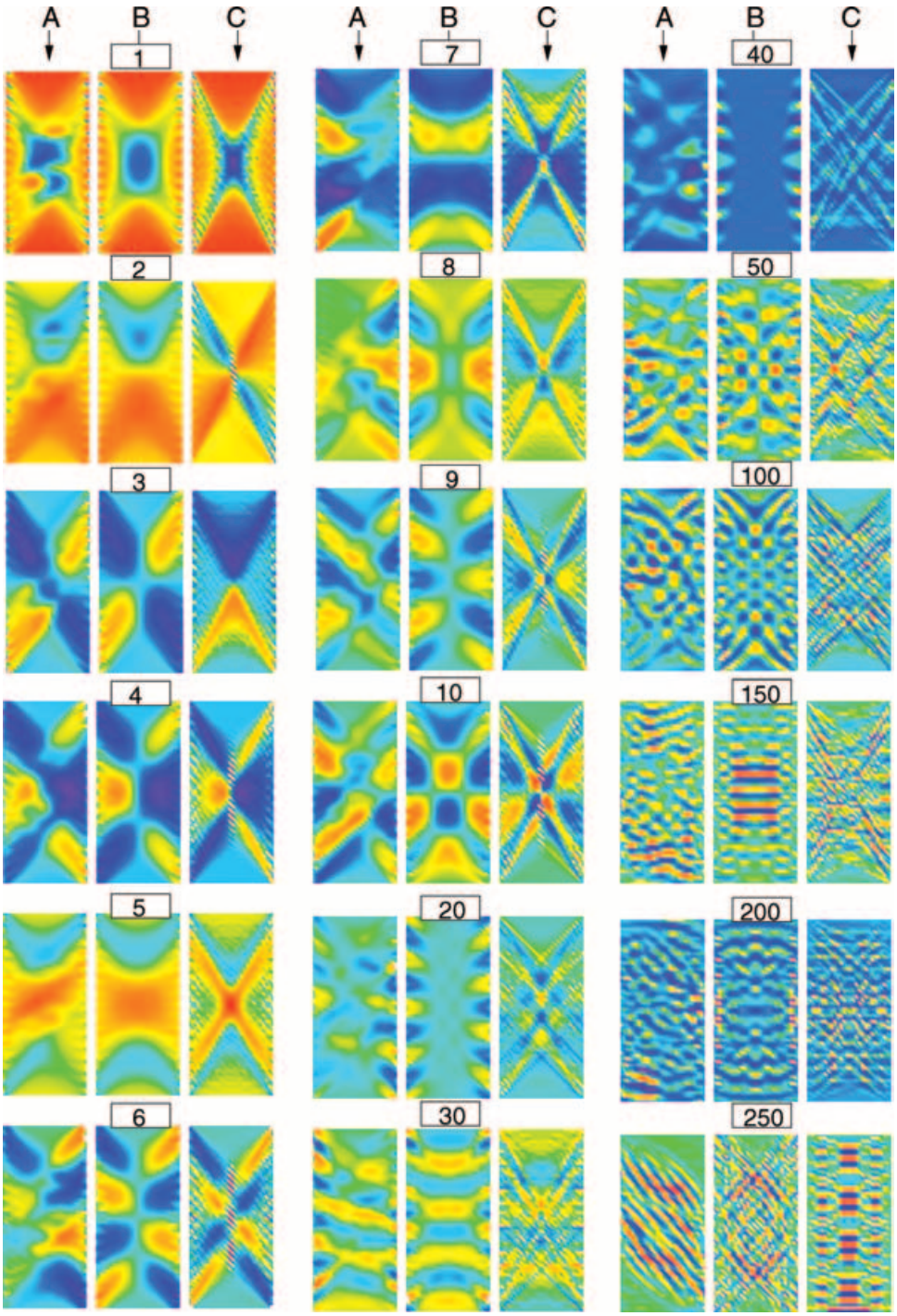

Figure 12. Full-waveform, Fresnel zone and straight-ray basis function (V_i) comparisons from SVD analysis. Columns A show the full-waveform basis functions computed about the solution. Columns B and C show the corresponding scattering theory and straight-ray basis functions respectively. The indices correspond to the singular values in Fig. 11 and the colour scale is constant for a given index.

measure of ray coverage, where the corresponding full-waveform and scattering theory basis functions are more localized and exhibit less X-pattern smearing typical of ray-based methods. With respect to the first J^{F} basis function, the first J^{FW} basis function is distorted displaying the effects of the heterogeneous background that are not accounted for in the scattering theory approximation. However, the full-waveform and scattering theory basis functions display a similar structure at each index. The straight-ray basis functions quickly become oscillatory and less localized and are dominated by the X-pattern feature. As the basis functions are scaled and added to construct the inverse estimates, the X-patterns transfer to the solution as artefacts. This suggests that the X-pattern artefacts persistent in many ray-based geophysical tomographic inversions are not only caused by limited aperture data collection geometries, but are exacerbated by the ray approximation. Based on the nature of the basis functions shown in Fig. 12 we would expect fewer of these artefacts

in the scattering theory solution even though the data collection geometry is the same in both cases. This X-pattern is also evident in higher-order scattering theory basis functions, but is more prevalent in the straight-ray case.

We used the finite-difference solution to compute the data for this case and added normally distributed noise with a standard deviation (S.D.) of 5 per cent of the maximum data value. To evaluate how well the predicted data fit the true data we use the chi-squared (χ^2) criterion

$$\chi^2 = \|W_{\mathrm{d}}(\delta D_{\mathrm{true}} - \delta D_{\mathrm{pred}})\|^2 \tag{49}$$

where $W_{\mathrm{d}}$is a diagonal matrix of 1/S.D., $\delta D_{\mathrm{true}}$is the true data and $\delta D_{\mathrm{pred}}$is the predicted data. When the data are appropriately fitted the expected value of $\chi^2$is equal to the number of data points, which is 256 in this case. Fig. 13 shows the χ^2value versus truncation index for the truncated scattering theory and straight-ray SVD solutions. The χ^2prediction errors decrease more quickly with truncation index in the scattering theory inversion, indicating that the Fresnel zone inversion is able to fit the data with fewer high-order oscillatory basis functions, limiting the build-up of artefacts. This is also evident in the singular value spectrum. The clustering of singular values for the straight-ray case would indicate that if the singular value magnitude corresponding to the noise level is below this clustering then high-index oscillatory basis functions would contribute to the solution. However, the decay of the singular values in the scattering theory case indicates that given the same singular value magnitude, the Fresnel zone solution would introduce fewer high-index oscillatory basis functions in the solution, reducing the build-up of artefacts. This is intuitively appealing since the physics of EM wave propagation are better represented by the Fresnel zone sensitivity distribution. Thus a smaller number of good basis functions are able to fit the data better than a larger number of poor basis functions.

Fig. 14 shows the construction of the SVD solutions for each method at several truncation indices. The magnitude of the conductivity difference values is immediately evident. The straight-ray solutions underpredict true conductivity difference values. As discussed previously, these estimates are too low because the ray path sensitivities are too large. Low ray-based inverse estimates were also noted by Holliger & Bergmann (2002) who used synthetic data and ray-based inversions to estimate attenuation coefficient values for a known model. The scattering theory solutions also underpredict the true values, but to a lesser degree. With respect to spatial resolution the scattering solution is able to distinguish between the two centre anomalies while the straight-ray solution is unable to localize the two peaks. The scattering solutions also resolve the upper anomaly more effectively, while the straight-ray solution tends to smear the boundaries and obscure the peak. The boundaries of the straight-ray estimates are expanded with respect to the true solution because ray theory does not account for the sensitivities of cells adjacent to the rays. This is particularly evident for smaller-scale features such as the anomaly at approximately 5 m depth in Fig. 9(a). Although somewhat hidden by the colour scale, the straight-ray solutions are more significantly marked by X-pattern artefacts as expected. As the truncation indices increase toward the target index for each method, the scattering theory solutions become more resolved while the straight-ray solutions change slowly and are unable to resolve the three separate peaks.

We have shown that under conditions common to georadar tomographic surveys, the physics of wave propagation represented by J^{F} are more accurate than the physics represented by J^{S}. This physical improvement results in more resolved tomograms, both in terms of the magnitude and spatial distribution of bulk conductivity changes. But how well do inverse tomographic estimates using J^{F} compare with the best possible estimates we might obtain by using a Jacobian matrix with insignificant sensitivity errors such as J^{FW}? We could answer this question for our synthetic example by conducting the full-waveform inversion using the finite-difference solution to compute J^{FW}. The full-waveform solution would probably require several iterations, each with an update of J^{FW}. We computed J^{FW} on the Beowulf cluster at Boise State University. The computation of J^{FW} for a single iteration required 1.5 days of parallel computation time on 100 2.4 GHz Pentium IV processors. Thus we deemed the full inversion an excessive computational burden. In contrast, computation of J^{F} for our synthetic problem only required approximately 10 min on an single processor machine running a 2.2 GHz Pentium IV processor. This represents immense computational savings at the expense of losing some accuracy in the sensitivity approximations. Although the full-waveform solution was not computed, comparison of the basis functions and singular values for J^{F} and J^{FW} gives insight into the accuracy lost by approximating J^{FW} with J^{F}. Although the effects of heterogeneity in $\delta\sigma(\mathbf{r})$ are evident in the full-waveform basis functions, the full-waveform and scattering theory basis functions display similar properties in terms of shape and magnitude. In addition, the singular value spectra for each case are nearly identical. When the inverse estimates are constructed, we have similar basis functions being scaled by similar singular values and added to construct the solutions. Thus, the inverse estimates provided by J^{F} will probably be similar to those provided by J^{FW} with a significant decrease in computational effort.

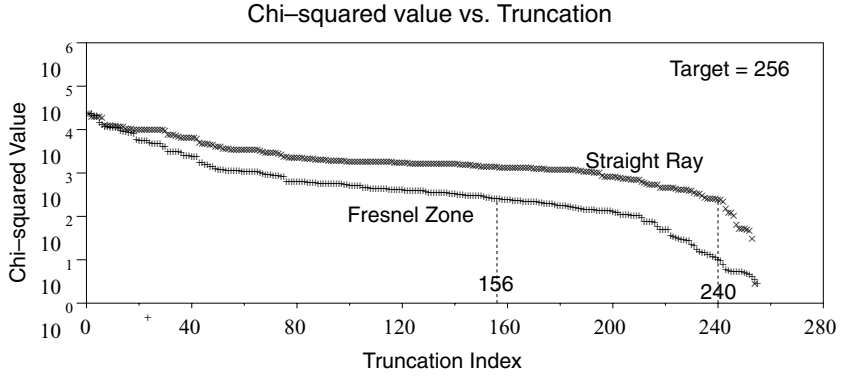

Figure 13. Comparison of Fresnel zone and straight-ray χ^2 values versus truncation index. Normally distributed noise was added to data with a standard deviation of 5 per cent of the maximum data value. The data are appropriately fitted when χ^2 reaches a target value of 256.

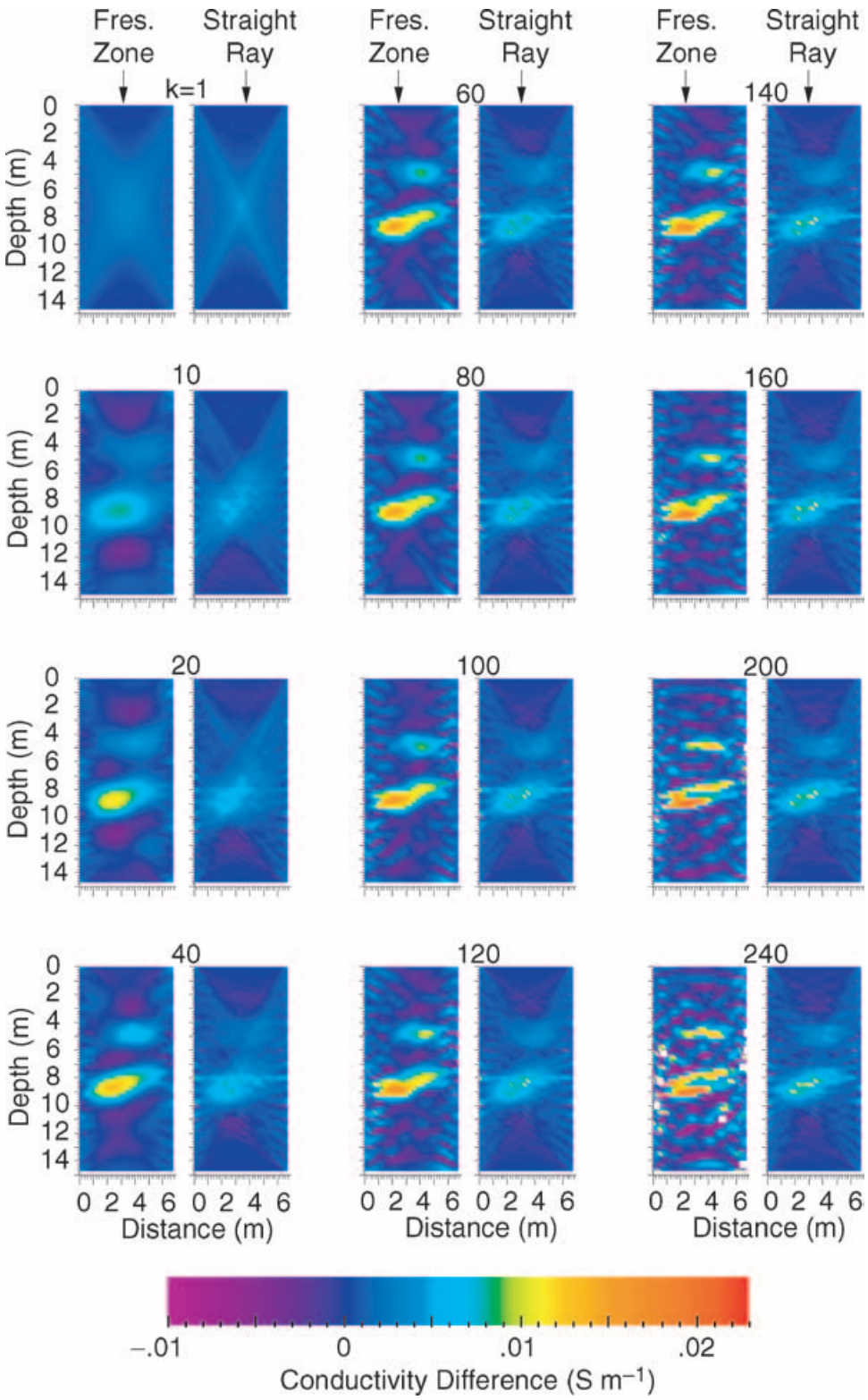

Figure 14. Fresnel zone and straight-ray SVD solutions versus truncation index.

5 CONCLUSION

We have presented an efficient method of approximating Fresnel volume sensitivity distributions for use in georadar attenuation-difference tomography in environments where dielectric contrasts are small and ray representations of wave propagation are straight. The characteristics of these distributions are similar to those shown by Marquering *et al.* (1999) in seismic propagation problems, but for a different reason. Namely, the distributions display the paradoxical result that the Fresnel volume sensitivities are zero along the ray

path. We have included in the approximation the effects of radiation patterns and have shown that radiation patterns affect attenuation-difference data and are important in attenuation-difference tomography. The SVD analysis provided several interesting insights into common observations in ray-based inverse estimates. In particular, ray-based basis functions tend to impose the X-pattern artefact on the inverse solution. We have also shown with a data prediction example that the Fresnel zone forward model represents EM wave propagation better than the ray-based model. In the SVD analysis, we showed how this physical improvement in the forward model results in more accurate and better resolved inverse estimates of bulk conductivity changes. The physical improvement is most evident when comparing the scattering theory and the full-waveform model basis functions and singular values which display similar behaviour. When dielectric heterogeneity is insignificant, bulk conductivity changes are relatively small, and EM waves propagate under low-loss conditions, Fresnel volume sensitivities approximated with scattering theory can provide inverse estimates that are good approximations to the solutions provided by full-waveform inversions with a significant decrease in computational effort.

ACKNOWLEDGMENTS

We gratefully acknowledge the constructive review provided by Guust Nolet, who helped us clarify our discussion of the sensitivity distributions. A second anonymous reviewer also provided useful insights and comments and helped us correct a misconception concerning the Hankel function. Many thanks to Klaus Holliger for graciously allowing us to employ his finite-difference code in this project. Bill Clement, Tom Clemo and John Bradford also provided helpful comments. Funding for this work was provided by the Inland Northwest Research Alliance (PhD fellowship for TJ), Bechtel BWXT Idaho, LLC (contract 00036570), and EPA grant X-970085-01-0. Computations were performed on the geophysical computing system (NSF-EPSCoR grant no EPS0132626) at the Center for Geophysical Investigation of the Shallow Subsurface and the Beowulf cluster at Boise State University ('Development of Tools to Enable the Port of Software to a Beowulf Cluster', NSF-Major Research Infrastructure Award no 0321233). We would also like to thank James Nelson for his assistance with the parallel computers.

REFERENCES

Abramowitz, M. & Stegun, I., 1975. Handbook of mathematical functions, Dover Publications, New York, 9th edn.

Barrash, W., Knoll, M., Hyndman, D., Clemo, T., Reboulet, E. & Hausrath, E., 2003. Tracer/time-lapse radar imaging test at the Boise Hydrogeophysical Research Site, in *Proc. SAGEEP 2003 (San Antonio, TX)*, pp. 163–174, Environmental and Engineering Geophysical Society, Denver, CO.

Buursink, M., 2004. First-order characterization of electromagnetic propagation velocity at the Boise Hydrogeophysical Research site using borehole radar methods, in *Society of Exploration Geophysics International meeting,* Society of Exploration Geophysics, Denver, CO, USA.

Červený, V. & Soares, J., 1992. Fresnel Volume ray tracing, *Geophysics,* **57**(7), 902–915.

Copty, N. & Rubin, Y., 1995. A stochastic approach to the characterization of lithofacies from surface seismic and well data, *Water Resour. Res.,* **31**(7), 1673–1686.

Day-Lewis, F., Harris, J. & Gorelick, S., 2002. Time-lapse inversion of cross-well radar data, *Geophysics,* **69**(6), 1740–1752.

Goldstein, S., 2004. Cross-well radar attenuation-difference tomography to monitor a bromide tracer test. *Masters Thesis,* Boise State University.

Golub, G.H. & Van Loan, C.F., 1983. *Matrix Computations,* Johns Hopkins University Press, Baltimore, MD.

Hagedoorn, T.G., 1954. A process of seismic reflection interpretation. *Geophysical Prospecting,* **2,** 85–127.

Holliger, K. & Bergmann, T., 1999. Finite-difference modeling of borehole georadar data, in *Proc. 69th Annual International Meeting of the Society of Exploration Geophysicists,* pp. 457–460, Society of Exploration Geophysicists, Tulsa, OK.

Holliger, K. & Bergmann, T., 2002. Numerical modeling of borehole georadar data, *Geophysics,* **67**(04), 1249–1257.

Holliger, K., Musil, M. & Maurer, H., 2001. Ray-based amplitude tomography for crosshole georadar data: what does it tell us?, in *Proc. 71st Annual International Meeting of the Society of Exploration Geophysicists,* pp. 1357–1360, Society of Exploration Geophysicists, Tulsa, OK.

Hubbard, S. & Rubin, Y., 2000. Hydrogeological parameter estimation using geophysical data: a review of selected techniques, *Contam. Hydrol.,* **45,** 3–34.

Hung, S., Dahlen, F. & Nolet, G., 2001. Wavefront healing: a banana-doughnut perspective, *Geophys. J. Int.,* **146,** 289–312.

Hyndman, D., Harris, J. & Gorelick, S., 1994. Coupled seismic and tracer test inversion for aquifer property characterization, *Water Resour. Res.,* **30**(7), 1965–1977.

Ishimaru, A., 1978. *Wave Propagation and Scattering in Random Media,* Academic Press, New York.

Jackson, J., 1999. *Classical Electrodynamics,* 3rd edn, John Wiley, New York.

Kravstov, Yu.A. & Orlov, Yu.I. 1980. Geometric optics of inhomogeneous media: Nauka, Moscow (in Russian).

Lane, J., Wright, D. & Haeni, P., 1999. Borehole radar tomography using saline tracer injections to image fluid flow in fractured rock, in *Proc. USGS Toxic Substances Hydrology Meeting, March 8–12,* United States Geological Survey, Charleston, SC.

Luo, Y. & Schuster, G.T., 1991. Wave-equation traveltime inversion, *Geophysics,* **56**(5), 645–653.

Marquering, H., Dahlen, F. & Nolet, G., 1999. Three-dimensional sensitivity kernels for finite-frequency traveltimes: the banana-doughnut paradox, *Geophys. J. Int.,* **137,** 805–815.

Nolet, G., 1987. Seismic wave propagation and seismic tomography, in *Seismic Tomography with Applications in Global Seismology and Exploration Geophysics,* pp. 1–23, ed. Nolet, G., Reidel, Dordrecht.

Peterson, J., 2001. Pre-inversion corrections and analysis of radar tomographic data, *J. Environ. Eng. Geophys.,* **6,** 1–18.

Spetzler, J. & Snieder, R., 2004. The Fresnel volume and transmitted waves, *Geophysics,* **69**(3), 653–663.

Stark, P. & Nikolayev, D., 1993. Toward tubular tomography, *J. geophys. Res.,* **98**(B5), 8095–8105.

Vasco, D. & Majer, E., 1993. Wavepath traveltime tomography, *Geophys. J. Int.,* **115,** 1055–1069.

Vasco, D.W., Peterson, J.E. & Majer, E.L. 1995. Beyond ray tomography: wavepaths and Fresnel volumes. *Geophysics,* **60**(6), 1790–1804.

Ward, S.H. & Hohmann, G.W., 1988. Electromagnetic theory for geophysical applications, in *Electromagnetic Methods in Applied Geophysics,* Vol. 1, pp. 131–312, ed. Nabighian, M.N., Society of Exploration Geophysicists, Tulsa, OK.

Wielandt, E., 1987. On the validity of the ray approximation for interpreting delay times, in *Seismic Tomography with Applications in Global Seismology and Exploration Geophysics,* pp. 1–23, ed. Nolet, G., Reidel, Dordrecht.

Woodward, M.J., 1992. Wave-equation tomography, *Geophysics,* **57**(1), 15–26.

APPENDIX A:

The homogeneous Helmholtz equation for the electric field is given by

$$\nabla^2 \mathbf{E}(\mathbf{r}, \omega) + k^2 \mathbf{E}(\mathbf{r}, \omega) = 0 \tag{A1}$$

where $k^2 = \omega^2 \mu_0 \epsilon - i\omega\mu_0 \sigma$ is the wavenumber (or propagation constant). If $\sigma = 0$ then all currents are displacement currents and there is no energy lost through Ohmic dissipation. If $\sigma \neq 0$ then the ratio of displacement current flow to Ohmic current flow is described by the loss tangent which is given by

$$\tan\delta = \frac{\sigma}{\omega\epsilon}. \tag{A2}$$

The transition between EM diffusion and wave propagation occurs at approximately $\tan\delta = 1$. Wave propagation in the georadar regime is typically low-loss propagation defined by $\tan\delta \ll 1$.

The attenuation coefficient for a sinusoidally varying plane wave in the time domain is given by (Ward & Hohmann 1988)

$$\alpha = \omega\sqrt{\mu\epsilon}\left[\frac{1}{2}(\sqrt{1+(\tan\delta)^2} - 1)\right]^{1/2}. \tag{A3}$$

Under low-loss conditions, eq. (A3) may be approximated as (Jackson 1999, pp. 295–340)

$$\alpha \approx \frac{\sigma}{2}\sqrt{\frac{\mu}{\epsilon}} \tag{A4}$$

which indicates that the attenuation coefficient is independent of frequency in the low-loss regime. The relationships between eq. (A2) through (A4) for a particular case are illustrated in Fig. A1. The curves represent eq. (A3) for several different conductivity values. The '+' symbols show the transition frequencies where $\tan\delta = 1$ for each curve. The '×' symbols show the approximation given in eq. (A4) valid for the low-loss condition $\tan\delta \ll 1$.

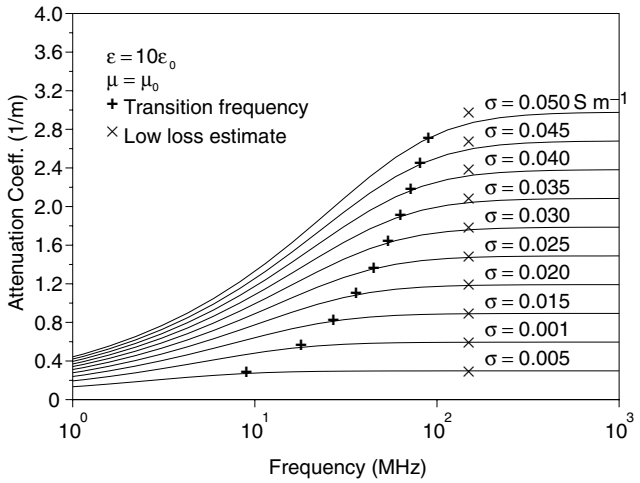

Figure A1. Relationship between attenuation coefficient and frequency in the georadar regime. The attenuation coefficient is frequency independent in the low-loss regime. Wave equation parameters chosen for this case are typical of those that might be found in a sand and gravel aquifer saturated with low-conductivity water.